frontiers | Frontiers in Earth Science

TYPE Original Research
PUBLISHED 04 January 2023
DOI 10.3389/feart.2022.1106168

OPEN ACCESS

EDITED BY
Yuwei Zhang,
Xi'an University of Architecture and Technology, China

REVIEWED BY
Guopeng Wu,
Lanzhou University of Technology, China
Yongting Duan,
Northeastern University, China

*CORRESPONDENCE
Zhijian Wu,
zhijianlz@163.com

SPECIALTY SECTION
This article was submitted to Environmental Informatics and Remote Sensing, a section of the journal *Frontiers in Earth Science*

RECEIVED 23 November 2022
ACCEPTED 09 December 2022
PUBLISHED 04 January 2023

CITATION
Wei T, Wu Z, Chen Y and Luo L (2023), Three-dimensional characterization and quantitative research of Malan loess microstructure under seismic loading. *Front. Earth Sci.* 10:1106168. doi: 10.3389/feart.2022.1106168

Three-dimensional characterization and quantitative research of Malan loess microstructure under seismic loading

Tingting Wei, Zhijian Wu*, Yanping Chen and Liang Luo

College of Transportation Science and Engineering, Nanjing Tech University, Nanjing, China

The deformation and failure of loess in areas of high seismic intensity are closely related to the dynamic vulnerability, which is primarily controlled by the loess microstructure. This study performed a series of dynamic triaxial tests and microstructure tests on intact loess to track and quantitatively characterize the evolution of the three-dimensional microstructure during deformation. The microstructural observations were performed using micro-CT on the samples after varying vibration times. The microstructure parameters (including pore radius, elongation, orientation, coordination number, pore throat area, and channel length) were obtained using a reconstructed pore network model. The results of this study demonstrated that the loess seismic subsidence originated from both compositional and microstructural characteristics. The intact loess had a loose structure with high porosity and limited cementation. Upon cyclic loading, cementation and contact breakdown led to the failure of the loess structure, followed by particle rearrangement. With increasing vibration times, the spaced and inter-aggregate pores became intra-aggregate pores, the pore throat size tended to decrease while the pore number tended to increase, the connectivity tended to weaken, and the shape tended to be long and flat. Pores >28 μm mainly provided spatial conditions for collapse deformation under seismic load. In addition, under the ultimate loading, large-volume cracks occurred inside the sample. The findings of this study provide further insights into loess seismic subsidence from the perspective of three-dimensional microstructures and a research basis for analyzing the stability of loess in relation to construction projects by combining finite and discrete elements.

KEYWORDS

Loess, microstructure, seismic subsidence, vibration time, quantitative analysis

Introduction

Loess is a Quaternary sedimentary soil widely distributed in Asia, Europe, America, and Africa (Wei et al., 2019a; Nan et al., 2021). In China, the loess covers an area of 631,000 km^2 (Wang et al., 2011). Moreover, the Loess Plateau, with an area >440,000 km^2, is the largest loess deposition area on earth (Meng et al., 2021). The engineering properties of soils are mainly controlled by their metastable microstructure, with less cement, higher porosity, and loose arrangement prone to liquefaction, subsidence, landslide, and other disasters due to earthquakes (Yuan and Wang, 2009; Juang et al., 2019; Zhang et al., 2022). Several strong earthquakes occurred in the loess region of China, all of which triggered seismic landslides, resulting in many casualties and high property damage (Sun et al., 2017; Zhuang et al., 2018). With the implementation of the "The Belt and Road Initiative", construction activities in loess areas are increasing, and it is especially important to clarify the dynamic properties of loess. Therefore, the study of microstructural changes of loess under dynamic loading will help to solve the engineering geological problems in loess areas.

Since the middle of the last century, scholars have applied low-precision microscopic equipment to explore loess microstructure (Matalucci et al., 1970; Cremaschi et al., 1990; Ma et al., 1998). Over time, studies on the microstructure of loess have progressed to a high-precision stage. SEM is widely used in the research of loess microstructure owing to its high precision and the ability to analyze mineral composition (Xie et al., 2018; Ni et al., 2020; Xu et al., 2020a). Quantitative data on loess particles and pore structure have been analyzed through SEM images to summarize the changes in pore quantity, area, and form corresponding to different dynamic loading stages (Li et al., 2018; Lian et al., 2022). The MIP technique is widely used in the study of loess pore size and collapsibility (Mu et al., 2020; Wang et al., 2021). Based on MIP tests, scholars have explored the impacts of different cycles on soil mechanics and pore characteristics, indicating that the cycling effects play a dominant role in the deterioration of loess engineering properties (Li et al., 2019; Wang et al., 2020). Micro-CT scans have been performed on saline intact loess to investigate the relationship between loess microstructure and hydraulic conductivity under freeze-thaw cycle conditions (Xu et al., 2020b). Based on the evaluation of the 3D pore structure of loess by X-ray scanning (Chen et al., 2019; Li and Shao, 2020), two different types of pores have been extracted, providing new research ideas on loess collapse (Yu et al., 2021). With the development of micron scanning equipment, research on loess microstructure is maturing. However, most studies have focused on two-dimensional parameters such as particle area distribution and pore area ratio. Research on the three-dimensional (3D) microstructure requires further exploration.

The integration of loess dynamic properties with loess microstructure has become a critical issue, with promising findings (Nan et al., 2021; Wang et al., 2021). To simulate the earthquake process, undisturbed loess is preloaded. Microstructure analysis has demonstrated that increasing dynamic stress amplitude aggravates soil microstructure deterioration (Li et al., 2019; Xu et al., 2021). The soil colloidal is damaged and the particle contact mode changes (Wang et al., 2011). Moreover, loading the loess leads to its transformation from a bimodal into a trimodal PSD, which defines three major pore series. However, the trimodal nature of PSD is destroyed under higher vertical stresses (Wang et al., 2020) and the loess grains are rearranged (Li et al., 2019). To quantitatively characterize the relationship between dynamic load frequency and loess microstructure, a series of dynamic triaxial tests and SEM scanning tests were conducted to establish the relationship between the dynamic characteristic and microscopic characteristic parameters of structural units (Wang et al., 2016; Kou et al., 2017; Zeng et al., 2022). The dynamic load type significantly affects the microstructure parameters of loess. Moreover, the diameter and direction probability entropy of these structural elements differ significantly under different wave loads (Chen et al., 2021). The study of loess microstructure has included the analysis of the amplitude, frequency, and waveform of the applied dynamic load. The loss of strength and deformation begins with the gradual change of microstructure. However, the continuous observation of the microstructure during cycling vibration is not enough to study the microstructure evolution.

The present study reconstructed a 3D pore network model of loess based on the analysis of 700 micro-CT images with a voxel size of 1 μm^3. The primary objective of this study was to characterize and quantitatively assess the evolution process of 3D loess microstructure under cyclic loading. The pore size, throat size, shape, and connectivity variation law of loess under different vibration times were evaluated. The results are expected to provide an in-depth and comprehensive understanding of loess microstructure and seismic subsidence behavior.

Experimental materials and methods

Material

The loess samples used in the study were Q_3 Malan loess collected from the Loess Plateau in the central-eastern part of Gansu Province (Figure 1). The samples were collected at 5 m in the Late Pleistocene strata, were undisturbed by engineering activity, showed a homogeneous distribution, and demonstrated few plant roots and wormholes.

The intact loess was cut into rectangles measuring approximately 25 cm × 25 cm× 15 cm. The samples were wrapped in many layers of cling film and shockproof film immediately after collection to preserve them without interference, with markings to indicate intact orientation. Table 1 shows the basic physical parameters of the collected loess. The particle size distribution of the intact loess is shown in Figure 2.

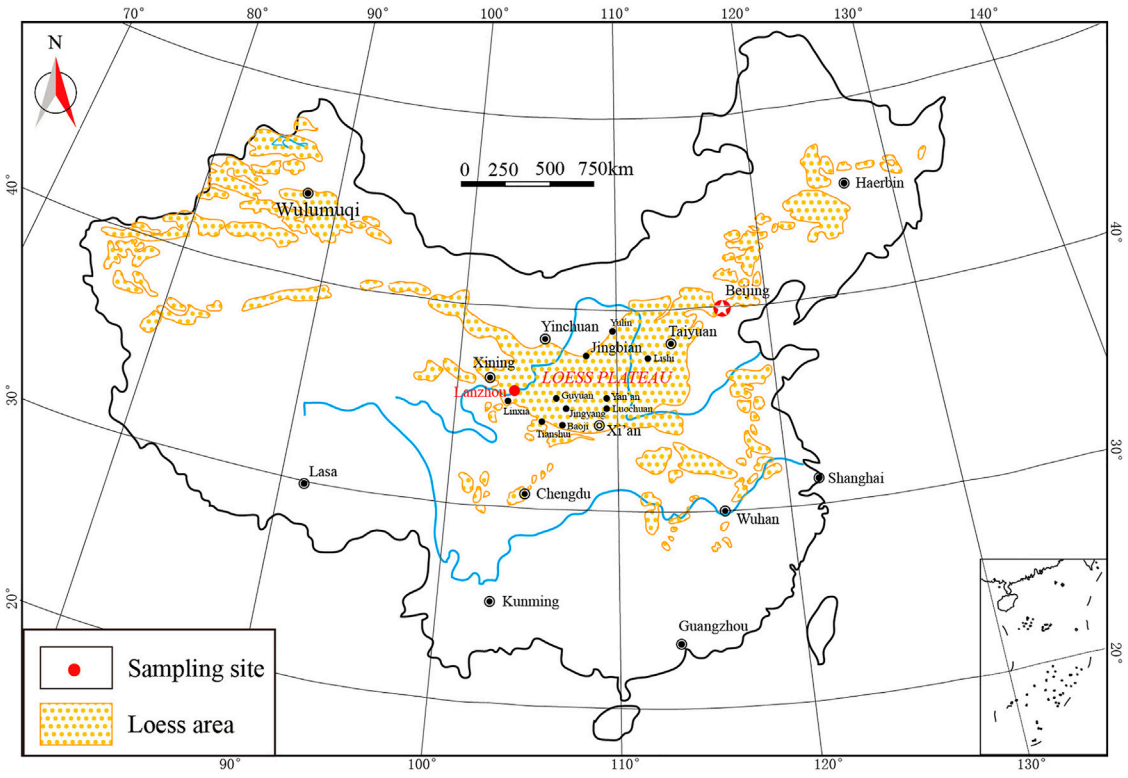

FIGURE 1
Sampling site of the studied loess.

TABLE 1 Physical property indices of the intact loess.

Dry density, ρ_d (g/cm^3)	Specific gravity, ρ (g/cm^3)	Saturation, S_r (%)	Porosity	Moisture content, ω (%)	Liquid limit, W_L (%)	Plastic limit, W_P (%)
1.33	2.71	5.73	0.51	2.2	29.59	20.73

Dynamic triaxial tests

These tests were performed utilizing the British GDS dynamic triaxial system to investigate the dynamic characteristics of the intact loess. Using a soil chipper and a cutter, samples of intact loess were produced in a standard size of φ50 mm×h100 mm.

The seismic load, as a random vibratory load, was reduced to an equal-amplitude sine wave load with cyclic loading in the analysis of the dynamic stress-strain relationship characteristics of loess, the frequency of which was set to 1 Hz. Before shearing, the intact loess samples were consolidated in the triaxial chamber until the changes in sample total volume remained stable (Nan, et al., 2021). This experiment addressed the effect of different cyclic vibrations of dynamic load on the dynamic properties of loess based on consolidation without drainage conditions. The consolidation ratio was K_C=1.0, the cell pressure was σ_3=100 kPa, and the dynamic load was σ_d=45 kPa. Considering a seismic fortification intensity in Lanzhou is 8°, the corresponding cyclic vibration times of the equivalent sine wave load were 20 times, and the cyclic vibration times of the dynamic load are set to 20, 150, and 300 times (or while the axial strain ε was >5%) (Figure 3).

Microstructure observation

After dynamic triaxial tests under default cyclic times (Figure 3), samples were collected from the center of the samples and scanned using an X-ray micro-CT scanner (Xradia 520 Versa, Zeiss) at the State Key Laboratory of

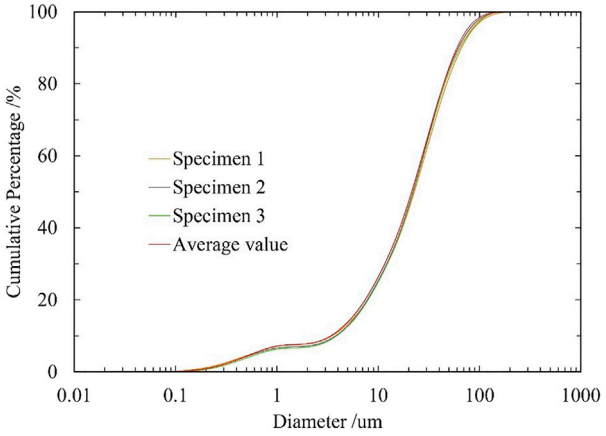

FIGURE 2
Particle size distribution of the loess used in the present study.

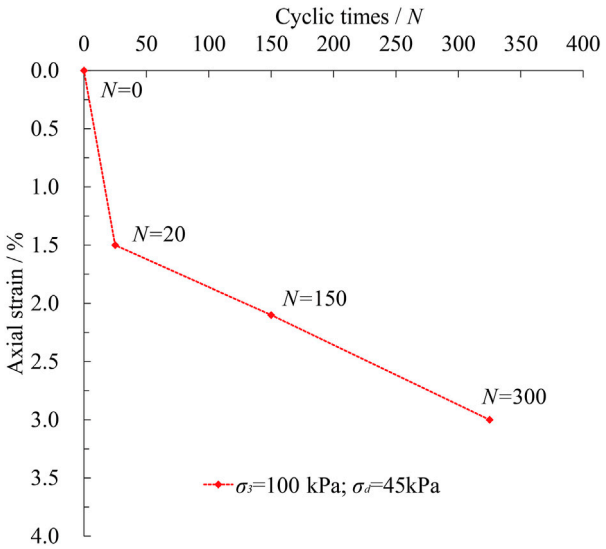

FIGURE 3
Deformation process of loess samples with cycling vibration and four microstructure observation sites.

Continental Dynamics (Figure 4). Five triaxial samples were cut from a single large block, and the microstructure scanning samples were collected from the center of the samples. The scanning samples were cylinders approximately 4 mm in diameter. During scanning, the voltage and current were set to 50 kV and 81 μA, respectively. The scanning range was 2000 × 2000 ×2000 voxels and the resolution was 1 μm for each pixel in this study. After scanning, 2000 16-bit images in the XY plane for each sample were obtained at 1-μm spacing between adjacent images.

3D microstructure reconstruction and characterization

The serial images obtained by micro-CT scanning were imported into Avizo software (FEI Company, France) to reconstruct the 3D microstructure. First, the images were preprocessed using the non-local means filter to eliminate noise and smooth the images (Wei et al., 2019a) (Figure 5A). Then, an appropriate threshold was selected to segment the pores and particles. The blue areas are pores in Figures 5B–E. Small holes in pores often lead to excessive separation during pore segmentation. Thus, the holes were filled with the appropriate values (Wei et al., 2020). Next, a watershed algorithm was used to split the pores into a set of connected and individually numbered pore bodies (Figure 5F). The watershed algorithm assumed the color value of the image as the elevation, simulated the flooding process, and segmented the region according to the watershed lines. Figure 6 shows the segmented results of four randomly selected slices from the intact loess. Finally, the pore network model (PNM) was generated based on the separated pores. The pore structure was characterized using a ball-stick model in which the balls represented pores bodies and the sticks represented the throats between two adjacent pores (Wei et al., 2019a) (Figures 5G, H).

Quantitative parameters

A cubic region of interest of 700×700×700 voxels was selected to calculate the pore microstructure parameters (Wei et al., 2019a). 3D porosity (n) was defined as the total number of pore voxels within the volume of interest divided by the total number of voxels of the volume. The equivalent radius (r_n) was defined as the radius of a sphere with a volume equal to the pore volume. The equivalent pore-throat area (A_b) was the radius of the thinnest contact position between two connected pore bodies. The channel length (*CL*) was defined as the length of the bond between two connected node centers, indicating the distance between two pore bodies. The orientation (*O*) was the angle between the short axis of the pore body and the horizontal plane. Pore elongation (*EL*) referred to the ratio of the short axis to the long axis of a pore body, ranging from 0 to 1. The smaller the value, the more elongated the pore. The coordination number (*CN*) was used to describe the connectivity of the pore structure, which was defined as the number of pores surrounding and connecting to one pore.

Results

Figure 7 shows the PNM reconstructed from the X-ray micro-CT images and the 3D binarized volumes of the samples (intact, cycle vibration 20, 150, and 300 times) with separated pore 2D sections, and lists their major structural parameters including the porosity (*n*), average equivalent pore radius (r_n), average pore coordination number (*CN*), pore elongation (*EL*), pore short axis orientation (*O*),

average equivalent pore-throat area (A_b) and average pore-throat channel length (CL).

Pore size distribution

The ability of loess soil to resist deformation and damage depends on its microstructure characteristics. The pore size distribution can indicate the complex pore structure in far more detail than porosity alone, and is one of the main factors to influence the microstructure.

The average equivalent pore radius (r_n) gradually decreased from 13 μm to 10.15 μm with increasing vibration times and decreased by 21.92% when destruction occurred. The significant variations in pore size distribution are shown in Figure 7. For intact loess (N=0), 75.1% of pores had radii of 4–16 μm (Figure 8A), while 87.1% had diameters of 8–44 μm (Figure 8B). These pores included spaced pores and some

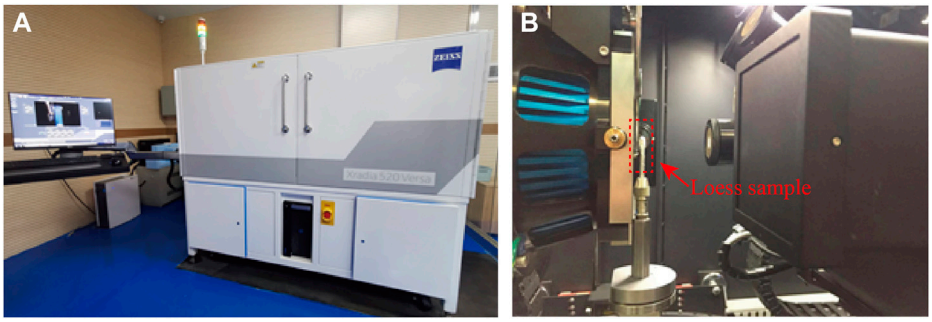

FIGURE 4
Micro-CT machine **(A)** and sample scanning stage **(B)**.

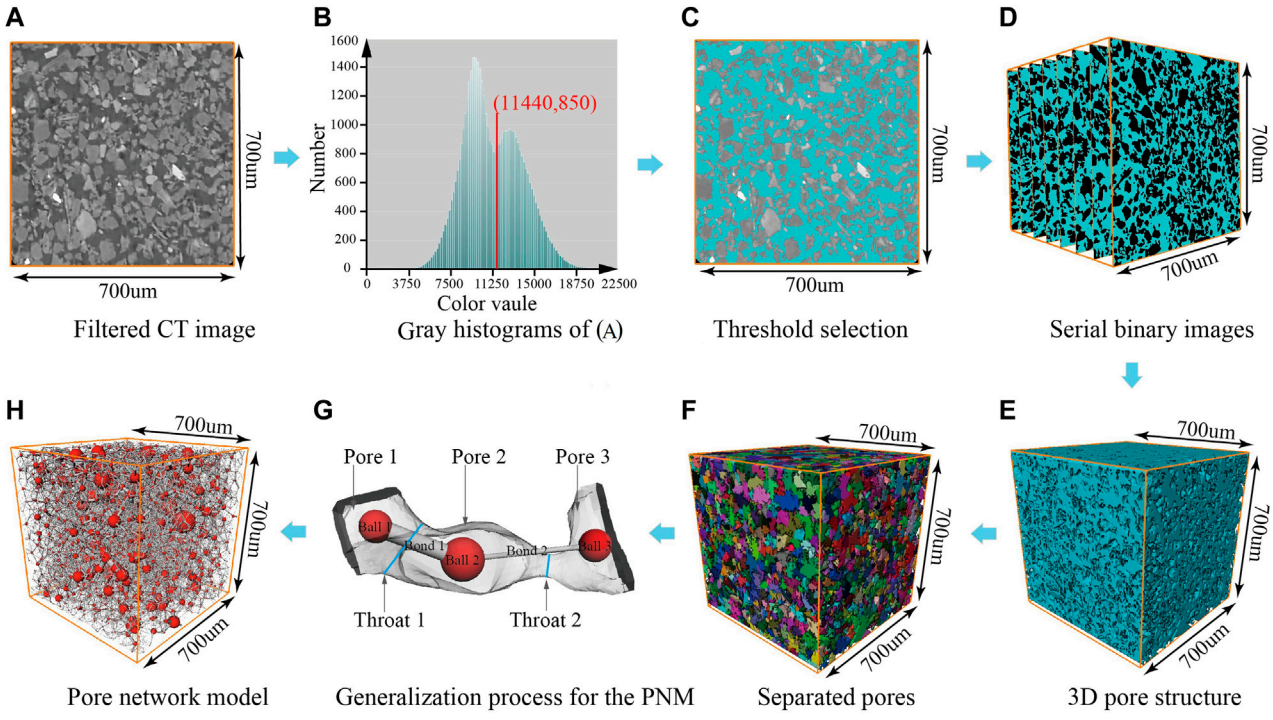

FIGURE 5
Reconstruction of the 3D PNM for pores in loess samples.

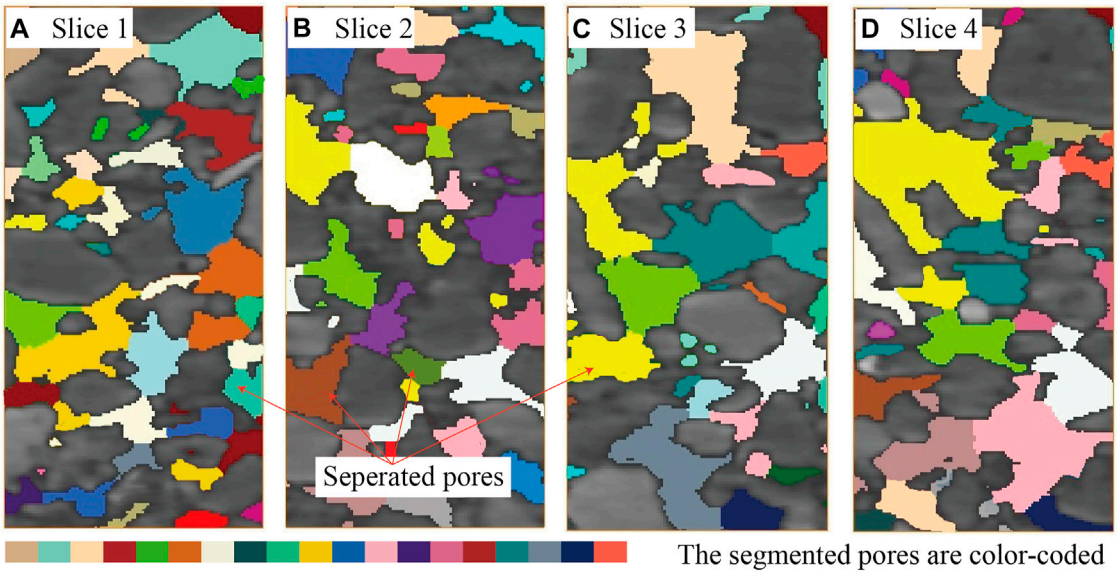

FIGURE 6
Pores segmented by the watershed algorithm.

Sample	*N*=0	*N*=20	*N*=150	*N*=300
3D pore	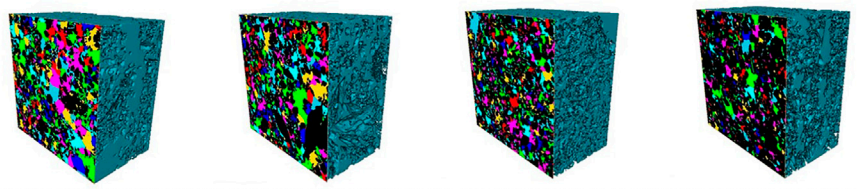			
	Size: 700 × 700 × 700 um; Voxel size (μm³): 1			
	Porosity *n*: 0.47	Porosity *n*: 0.40	Porosity *n*: 0.33	Porosity *n*: 0.31
PNM	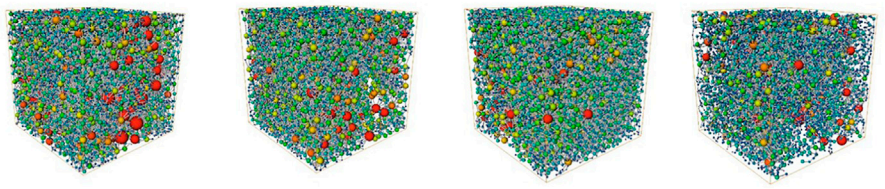			
	Average *CN*: 8.18	Average *CN*: 7.06	Average *CN*: 5.77	Average *CN*: 3.66
	Average r_n (μm): 13.00	Average r_n (μm): 12.35	Average r_n (μm): 10.75	Average r_n (μm): 10.15
	Average A_b (μm²): 132.21	Average A_b (μm²): 49.06	Average A_b (μm²): 42.11	Average A_b (μm²): 39.53
	Average *CL* (μm): 44.28	Average *CL* (μm): 43.74	Average *CL* (μm): 39.30	Average *CL* (μm): 40.26
	Average *EL*: 0.50:	Average *EL* : 0.49	Average *EL* : 0.47	Average *EL* : 0.45
	Average *O* (°): 57.88	Average *O* (°): 56.92	Average *O* (°): 58.27	Average *O* (°): 58.84

FIGURE 7
3D pore volumes and extracted PNMs with their characteristics.

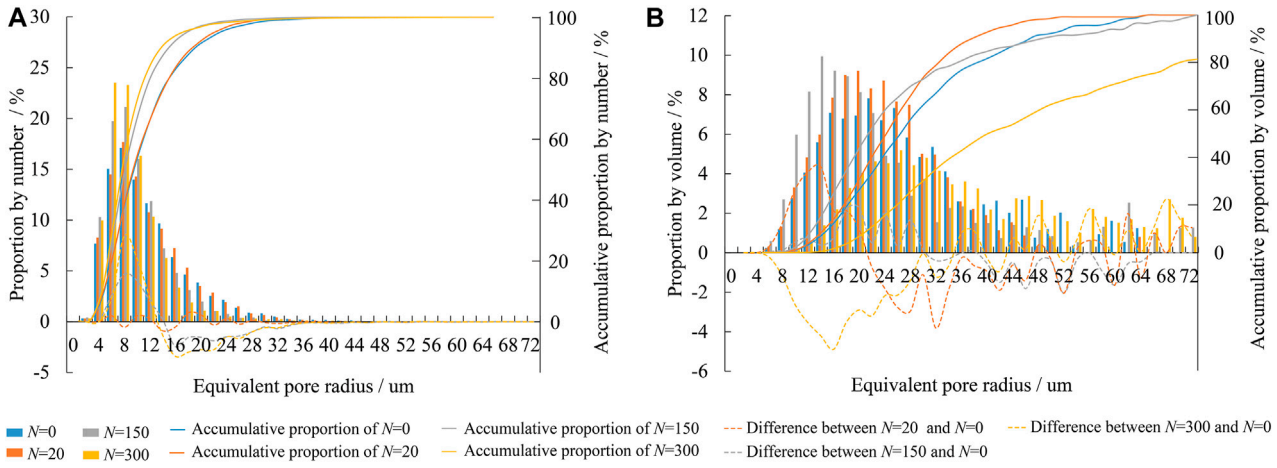

FIGURE 8
Pore size distributions. **(A)** Pore number distributions and the difference before and after loading. **(B)** Pore volume distributions and the difference before and after loading.

relatively large inter-particle pores (Wei et al., 2020). The peaks of pore number distribution for N=0, N=20, N=150, and N=300 were 17.1%, 17.7%, 21.1%, and 23.5% corresponding to pore equivalent radii of approximately 8 μm, 8 μm, 8 μm, and 6 μm, respectively. The larger the peak amplitude, the more concentrated the pore size distribution, indicating that the pore size distribution gradually concentrated with increasing vibration times (Figure 8A). The peaks of the pore volume distribution for N=0, N=20, N=150, and N=300 were 7.8%, 9.2%, 9.9%, and 5.2% corresponding to pore equivalent radii of approximately 22 μm, 18 μm, 12 μm, and 24 μm, respectively. From N=0 to N=150, the pore volume distribution gradually concentrated and shifted to smaller radii. However, N=300 showed the opposite trend (Figure 8B).

The differences in pore number and volume proportion among the four samples are plotted in Figures 8A, B. Overall, large pores showed decreased numbers and volumes, while small pores showed increases. The proportions of pores <14 μm increased by 13.6% and 17.9% in the samples after 150 and 300 vibration cycles, respectively. When N=20, the pore number change range was not obvious. Regarding pore volume change, the proportion of pores with radii <28 μm increased by 11.6% for N=20 and by 19.0% for N=150. However, pores with radii <28 μm decreased in volume by 32% for 300 cyclic loads.

The pore distributions and variations under cyclic loading reflect the process of loess subsidence. Spaced pores and some of the relatively large inter-particle pores decreased in number and volume and shifted to small inter-particle pores or intra-aggregate pores. However, after destruction, although the number of small pores increased, loose fracture zones were generated, resulting in an increased proportion of large pore volume (Figure 8B).

Pore throat

The pore throat is the thinnest part connecting two pore bodies, with the throat the channel connecting two pores. In the intact loess, the pore throat number was 8388 in the area of interest, the average pore-throat area was 132.21 μm^2, and the average channel length was 44.28 μm. For N=20, N=150, and N=300, the pore throat numbers were 8738, 9875, and 11,085; the average pore-throat areas were 49.06 μm^2, 42.11 μm^2, and 39.53 μm^2; and the average channel lengths were 43.74 μm, 39.30 μm, and 40.26 μm, respectively (Figure 7). Figure 9 depicts the percentage distributions of pore throats for different throat areas and the difference among the four samples under different vibration times. For vibration times from 20 to 300, the number of pores with throat area >50 μm^2 decreased by 6%, 11%, and 13%, respectively, compared to the intact loess. Moreover, the proportion of those <50 μm^2 increased (Figure 9A). The number of pores with throat channel lengths >50 μm decreased by 9.6% when the loess was vibrated 20 times. When the loess was subjected to 150 and 300 cyclic vibrations, the number of pores >40 μm decreased by 13.7% and 18.0%, respectively (Figure 9B).

The results indicated that the loess structure is compressed during cyclic vibration loads and that large pores are transformed into many small pores, forming more pores and throats with smaller areas and channels. The effect was especially strong after 150 cyclic vibrations, in which the number of pores and throats was the largest, but the size was the smallest.

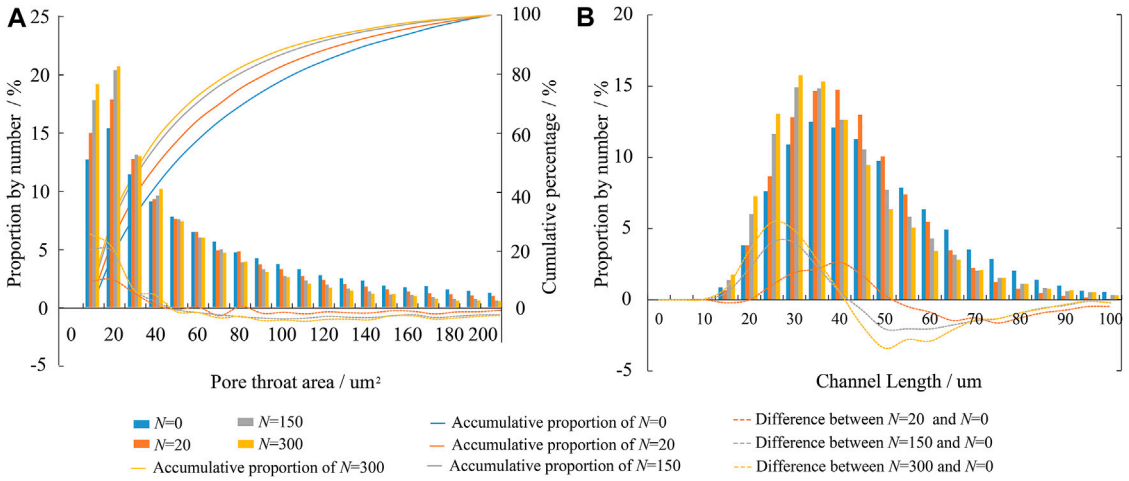

FIGURE 9
Pore-throat size distributions. **(A)** Pore-throat area distributions and the difference before and after loading. **(B)** Channel length distributions and the difference before and after loading.

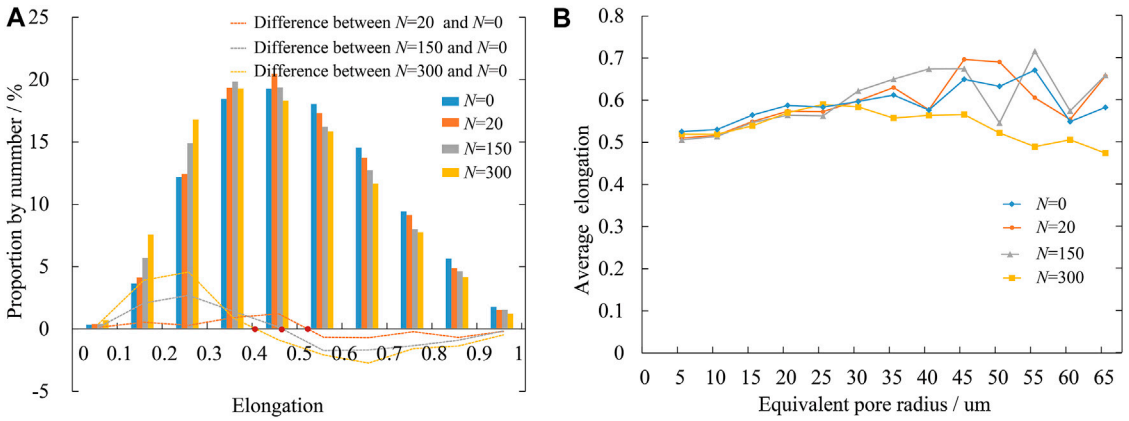

FIGURE 10
Pore elongation distribution. **(A)** Pore elongation distributions and the difference before and after loading. **(B)** Relationship between pore equivalent radius and elongation.

Pore elongation

Variation in pore elongation can reflect the microscopic deformation characteristics of the loess structure. The average pore elongation values of the four samples were 0.50, 0.49, 0.47, and 0.45, respectively (Figure 7). More than 98% of the pores showed elongation values between 0.1 and 0.9 in intact loess. The difference among the four samples is shown in Figure 10A. The turning point of elongation variation in the samples before and after loading was about 0.45. The number of pores smaller than this value increased by 3%, 6%, and 10%, respectively, while the number of pores above this value decreased correspondingly. These results indicated that the loess structure was compressed and that the pores gradually flattened under the action of cyclic load.

Figure 10B shows the average elongation of the pores according to the radius. For pores <28 μm in the four samples, the average elongation increased gradually with increasing pore radius. For pores >28 μm, the average elongation in the *N*=0, *N*=20, and *N*=150 samples showed varying elongation increases; however, the curve showed no obvious linear trend. In the *N*=300 sample, the average

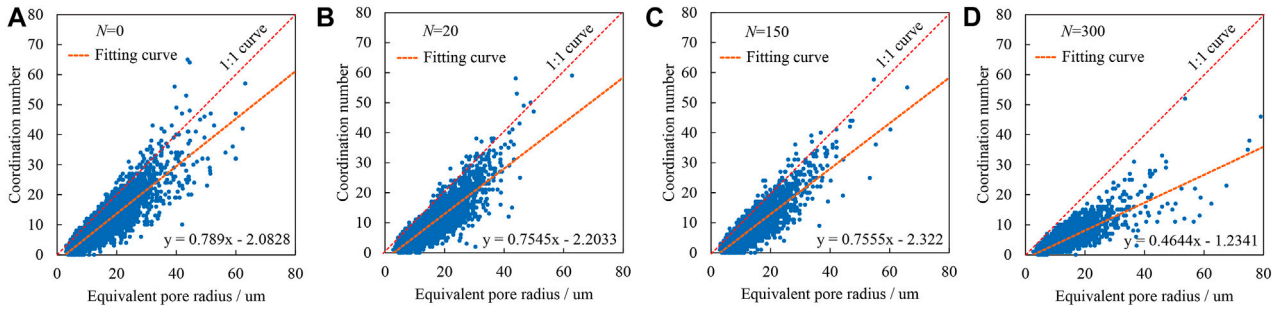

FIGURE 11
Coordination number distributions and the relationship between coordination number and equivalent radius.

elongation decreased significantly with the pore increase to >28 μm. These results indicated that the pores with a radius >28 μm are seriously deformed after being loaded and are pressed into a flat elongated shape. This result is consistent with the change in pore volume.

Pore connectivity

The average *CN* values were 8.18, 7.06, 5.77, and 3.66 for the *N*=0, *N*=20, *N*=150, and *N*=300 samples, respectively. *CN* can roughly reflect the weakening of pore connectivity in loess after loading. Figures 11A–D show the relationships between *CN* distributions and the equivalent pore radius of the four loess samples. With increased vibration times, the number of pores with *CN* >10 decreased significantly, especially when the vibration reached 300. Meanwhile, the fitting curve of *CN* distribution gradually deviated from the 1:1 curve, indicating that with increased vibration times, the *CN* of the same radius pore decreased. These findings demonstrated that although these pores were large, including those created after destruction, their connectivity was worse than that of pores of the same size in intact loess.

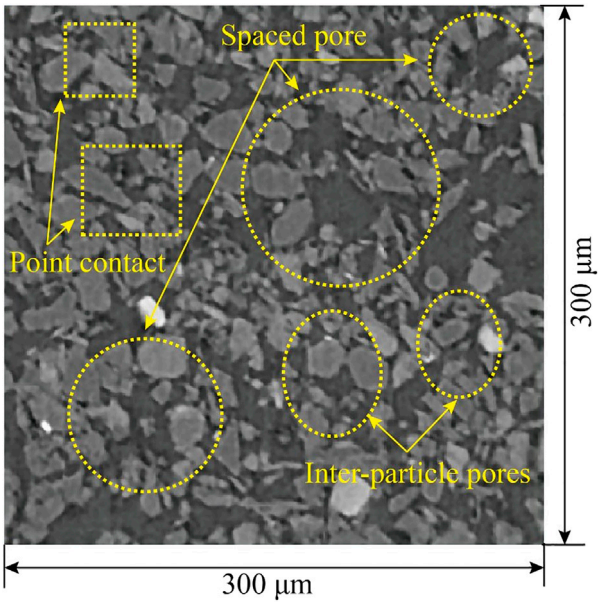

FIGURE 12
Overall microstructure of the intact loess shown in the CT 2D image.

Discussion

Occurrence of seismic subsidence

Regarding loess seismic subsidence, a critical challenge is associated with the transition from spaced and loosely packed to compacted and more stable structures. The Malan loess in the present study had a loose microstructure, with pores diameters of 8–44 μm predominating in the total volume at a proportion of 87.1% (Figure 8). These widely distributed spaced, inter-particle, and inter-aggregate pores are the main contributors to loess structural collapse (Lei Wang, 1987; Osipov and Sokolov, 1995). The spaced pores are formed by the stacking of particles, and their size is much larger compared to the surrounding particles (Figure 12). Clay particles <5 μm accounted for only 10% of the studied loess and acted as the main the cement, formed clay bridges and aggregates, and attached to the surface of the silt and sand (Wei et al., 2019b). These characteristics determined the weak cementation in the studied loess and the contact between particles was mainly point contact (Figure 12). The cohesion and internal friction under low water content supported the stability of the structural system, keeping the loess relatively stable in its intact state.

However, when subjected to cyclic loading, the weak cementation and direct point contact no longer function

effectively and consistently. When the external load exceeds the bond yield strength, the surrounding particles will break off at weak cementation points. The exfoliated particles will fall into the pore space, forming a new rearrangement structure (Nan et al., 2021). During this process, in terms of pore volume distribution, the collapse of pores >28 μm resulted in an increased number of small-sized pores and a decreased number of large-size pores (Figures 8–10). After the structure collapse, the loess was compressed, resulting in decreased pore-throat channel length and elongation, in addition to flat pore development (Figures 8–10). Under low confining pressure, cyclic loading disintegrated the local microstructure, resulting in structural loss and the generation of large pore cracks (Figure 8). Thus, the microstructural characteristics of loess, including pore types, contact relationship, and cementation degree, are internal factors related to its resistance to external loads.

Engineering applications and implications

Loess soil stability challenges exist in underground engineering, slope engineering, and foundations in loess regions (Liu et al., 2018; Juang et al., 2019; Liu et al., 2020). The process of loess deformation and instability is gradual, beginning with local microstructural changes that progressively produce microcracks, which then gradually expand into through-cracks, and finally, slope sliding. Alternatively, microstructure collapse may lead to a large area of uneven settlement, resulting in the instability of the foundation and surrounding tunnel rock. The results of this study showed that multiple dynamic loads can lead to significant changes in soil pore microstructure. The change in pore structure from loose to compact occurs mainly due to microstructure collapse and rearrangement. In some filling and tunnel projects, we can pre-treat the soil in advance to produce subsidence. Regarding earthquakes, the amount of seismic subsidence will be little or even none, thus reducing the amount and speed of deformation. The microstructure evolution can be applied to numerical simulations to simulate variations in local microstructure when combining finite and discrete elements. This new method more accurately simulates soil stability.

Conclusion

The seismic subsidence of loess is closely related to its microstructure. This study reconstructed the 3D microstructure based on micro-CT images with a voxel size of 1 μm^3. The PNM was also generated based on the 3D pore structure to extract quantitative pore parameters. By studying the evolution law of microstructures during cyclic vibration, the influence of seismic duration on microstructure can be studied to explore the microscopic mechanisms of seismic deformation. The results of the analysis led to the following major conclusions:

1) For the intact Malan loess in Lanzhou with low water content examined in this study, the high porosity of 0.51 and the small proportion of clay led to loose particle arrangement and weak cementation, which was mainly an unstable direct point contact. The spaced and inter-aggregate pores predominated the total pore volume.
2) Pore size was most sensitive to the cyclic loading; in the dynamic triaxial tests, the spaced and inter-aggregate pores transformed into intra-aggregate pores, the total number of pore throats and channels increased but the connectivity decreased; and the pores were flatter, indicating pore compression. Pores >28 μm mainly provide spatial conditions for collapse deformation under seismic load.
3) Loess seismic subsidence originates from both compositional and microstructural characteristics. The former primarily involve the clay and water content, which directly affects the particle arrangement and bonding strength. The latter primarily involve the volume content of spaced and inter-aggregate pores and contact relationships.
4) The microstructure characterization and evolution of loess during seismic loading can be applied to the numerical simulation. The combination of finite and discrete elements to simulate slope stability can better restore the slope instability process from local structural variation gradually expanding to a large range.

Future work will focus on seismic amplitude and frequency to analyze the influence of seismic factors on the microstructure and microstructure sensitivity to seismic factors, to reveal in depth the microscopic mechanism of loess subsidence.

Data availability statement

The raw data supporting the conclusion of this article will be made available by the authors, without undue reservation.

Author contributions

TW was responsible for the study concept and manuscript writing. ZW was responsible for the study concept and resources. YC performed the

experiments. LL was responsible for editing the manuscript draft.

Funding

This work was supported by the National Natural Science Foundation of China (grant numbers 42102305 and U1939209) and the Six Talent Peaks Project of Jiangsu Province (JZ-016).

Acknowledgments

All authors thank the constructive review of the reviewer and editor for the early version of the manuscript.

Conflict of interest

The authors declare that the research was conducted in the absence of any commercial or financial relationships that could be construed as a potential conflict of interest.

Publisher's note

All claims expressed in this article are solely those of the authors and do not necessarily represent those of their affiliated organizations, or those of the publisher, the editors, and the reviewers. Any product that may be evaluated in this article, or claim that may be made by its manufacturer, is not guaranteed or endorsed by the publisher.

References

Chen, H. E., Shan, W. C., and Jiang, Y. L. (2021). Dynamic characteristics of xianyang loess based on microscopic analysis: A quantitative evaluation. *B. Eng. Geol. Environ.* 80 (10), 8247–8263. doi:10.1007/s10064-021-02432-x

Chen, S. J., Ma, W., and Li, G. Y. (2019). Study on the mesostructural evolution mechanism of compacted loess subjected to various weathering actions. *Cold Reg. Sci. Technol.* 167 (1), 102846. doi:10.1016/j.coldregions.2019.102846

Cremaschi, M., Fedoroff, N., Guerreschi, A., Huxtable, J., Colombi, N., Castelletti, L., et al. (1990). Sedimentary and pedological processes in the upper pleistocene loess of northern Italy. the bagaggera sequence. *Quatern. Int.* 5, 23–38. doi:10.1016/1040-6182(90)90022-V

Juang, C. H., Dijkstra, T., Wasowski, J., and Meng, X. (2019). Loess geohazards research in China: Advances and challenges for mega engineering projects. *Eng. Geol.* 251, 1–10. doi:10.1016/j.enggeo.2019.01.019

Kou, X. H., Zhang, Q., and Dong, X. Q. (2017). Study on dynamic characteristics of acid compacted loess under different vibration frequencies. *Nat. Sci. Ed.* 38 (2), 249–254. doi:10.3969/j.issn.1673-3193.2017.02.027

Lei, X. Y., and Wang, S. F. (1987). Size of loess pores in relation to collapsibility. *Hydrogeol. Eng. Geol.* 14 (5), 15–18.

Li, P., and Shao, S. (2020). Can X-ray computed tomography (CT) be used to determine the pore-size distribution of intact loess. *Environ. Earth Sci.* 79 (1), 29–12. doi:10.1007/s12665-019-8777-z

Li, P., Xie, W. L., Pak, R., and Vanapalli, S. K. (2018). Microstructural evolution of loess soils from the loess plateau of China. *Catena* 173, 276–288. doi:10.1016/j.catena.2018.10.006

Li, T. L., Fan, J. W., Xi, Y., Xie, X., and Hou, X. K. (2019). Analysis for effect of microstructure on swcc of compacted loess. *J. Eng. Geol. Chin.* 27 (5), 045. doi:10.13544/j.cnki.jeg.2019045

Lian, B. Q., Wang, X. G., Zhan, H. B., Wang, J., Peng, J., Gu, T., et al. (2022). Creep mechanical and microstructural insights into the failure mechanism of loess landslides induced by dry-wet cycles in the Heifangtai platform, China. *Eng. Geol.* 300, 106589. doi:10.1016/j.enggeo.2022.106589

Liu, N. F., Li, N., Li, G. F., Zhang, Z. Q., and Mu, Y. M. (2018). Deformation and collapse mechanisms of water-rich soil tunnels. *Soil Mech. Found. Eng.* 54 (6), 384–394. doi:10.1007/s11204-018-9485-5

Liu, N. F., Li, N., Xu, C. B., Li, G. F., Song, Z. P., and Yang, M. (2020). Mechanism of secondary lining cracking and its simulation for the dugongling tunnel. *Rock Mech. Rock Eng.* 53, 4539–4558. doi:10.1007/s00603-020-02183-3

Ma, W., Cheng, G. D., Zhu, Y. L., and Xu, X. Z. (1998). The state key laboratory of frozen soil engineering: Review and prospect. *J. Glaciol. Geocryol.* 4, 1–10.

Matalucci, R. V., Abdel-Hady, M., and Shelton, J. W. (1970). Influence of microstructure of loess on triaxial shear strength. *Eng. Geol.* 4 (4), 341–351. doi:10.1016/0013-7952(70)90024-4

Meng, Z. J., Ma, P. H., and Peng, J. B. (2021). Characteristics of loess landslides triggered by different factors in the Chinese loess plateau. *J. Mt. Sci-Engl.* 18 (12), 3218–3229. doi:10.1007/s11629-021-6880-6

Mu, Q. Y., Zhou, C., and Ng, C. W. W. (2020). Compression and wetting induced volumetric behavior of loess: Macro- and micro-investigations. *Transp. Geotech.* 23, 100345. doi:10.1016/j.trgeo.2020.100345

Nan, J. J., Peng, J. B., Zhu, F. J., Ma, P. H., Liu, R., Leng, Y. Q., et al. (2021). Shear behavior and microstructural variation in loess from the Yan'an area, China. *Eng. Geol.* 280, 105964. doi:10.1016/j.enggeo.2020.105964

Ni, W. K., Yuan, K. Z., Lü, X. F., and Yuan, Z. H. (2020). Comparison and quantitative analysis of microstructure parameters between original loess andremoulded loess under different wetting-drying cycles. *Sci. Rep-UK* 10 (1), 5547–5612. doi:10.1038/s41598-020-62571-1

Osipov, V. I., and Sokolov, V. N. (1995). Factors and mechanism of loess collapsibility. *Genesis Prop. collapsible soils* 6, 49–63. doi:10.1007/978-94-011-0097-7_4

Sun, P., Li, R. J., Jiang, H., Lgwe, O., and Shi, J. S. (2017). Earthquake-triggered landslides by the 1718 tongwei earthquake in gansu province, northwest China. *B. Eng. Geol. Environ.* 76, 1281–1295. doi:10.1007/s10064-016-0949-4

Wang, F., Li, G., Ma, W., Mu, Y., Zhou, Z. W., Zhang, J., et al. (2020). Effect of repeated wetting-drying-freezing-thawing cycles on the mechanic properties and pore characteristics of compacted loess. *Adv. Civ. Eng.* 1, 1–8. doi:10.1155/2020/8839347

Wang, H. B., Zhou, B., Wu, S. R., Shi, J. S., and Li, B. (2011). Characteristic analysis of large-scale loess landslides: A case study in baoji city of Loess Plateau of northwest China. *Nat. Hazard Earth. Sys.* 11 (7), 1829–1837. doi:10.5194/nhess-11-1829-2011

Wang, J. D., Li, P., Ma, Y., Vanapalli, S. K., and Wang, X. G. (2020). Change in pore-size distribution of collapsible loess due to loading and inundating. *Acta Geotech.* 15 (5), 1081–1094. doi:10.1007/s11440-019-00815-9

Wang, N. Q., Luo, D. H., Yao, Y., Chen, X. X., and Yang, J. G. (2011). Dynamic strength and Microstructure change of Malan loess under triaxal cyclic loading. *J. Eng. Geol. Chin.* 19, 467–471. doi:10.1007/s12182-011-0118-0

Wang, Q., Zhong, X. M., Su, Y. Q., Li, N., Che, G. F., and Wang, L. L. (2016). Study of the dynamic deformation properties of loess under a dynamic load in the Lanzhou Metro. *Mod. Tunn. Tech.* 53, 137–142. doi:10.13807/j.cnki.mtt.2016.06.019

Wang, Y., Yang, H., and Jing, X. (2021). Structural characteristics of natural loess in northwest China and its effect on shear behavior. *Geotech. Geol. Eng.* 39 (1), 65–78. doi:10.1007/s10706-020-01420-4

Wei, T. T., Fan, W., Yu, N. Y., and Wei, Y. N. (2019a). Three-dimensional microstructure characterization of loess based on a serial sectioning technique. *Eng. Geol.* 261, 105265. doi:10.1016/j.enggeo.2019.105265

Wei, T. T., Fan, W., Yuan, W. N., Wei, Y. N., and Yu, B. (2019b). Three-dimensional pore network characterization of loess and paleosol stratigraphy from

south Jingyang plateau, China. *Environ. Earth. Sci.* 78 (11), 333. doi:10.1007/s12665-019-8331-z

Wei, Y. N., Fan, W., Yu, B., Deng, L. S., and Wei, T. T. (2020). Characterization and evolution of three-dimensional microstructure of Malan loess. *Catena* 192, 104585. doi:10.1016/j.catena.2020.104585

Xie, W. L., Li, P., Zhang, M. S., Cheng, T. E., and Wang, Y. (2018). Collapse behavior and microstructural evolution of loess soils from the loess plateau of China. *J. Mt. Sci-Engl.* 15, 1642–1657. doi:10.1007/s11629-018-5006-2

Xu, J., Li, Y. F., Ren, C., Wang, S. H., Vanapalli, S. K., and Chen, G. (2020b). Influence of freeze-thaw cycles on microstructure and hydraulic conductivity of saline intact loess. *Cold Reg. Sci. Technol.* 181, 103183. doi:10.1016/j.coldregions.2020.103183

Xu, J., Li, Y. F., Ren, C., and Wei, L. (2020a). Damage of saline intact loess after dry-wet and its interpretation based on sem and nmr. *Soils Found.* 60 (4), 911–928. doi:10.1016/j.sandf.2020.06.006

Xu, J., Ren, C., Wang, S. H., Gao, J. Y., and Zhou, X. G. (2021). Permeability and microstructure of a saline intact loess after dry-wet cycles. *Adv. Civ. Eng.* 2021, 1–18. doi:10.1155/2021/6653697

Yu, B., Fan, W., Dijkstra, T. A., Wei, Y. N., and Deng, L. S. (2021). Heterogeneous evolution of pore structure during loess collapse: Insights from X-ray micro-computed tomography. *Catena* 201, 105206. doi:10.1016/j.catena.2021.105206

Yuan, Z. X., and Wang, L. M. (2009). Collapsibility and seismic settlement of loess. *Eng. Geol.* 105 (1-2), 119–123. doi:10.1016/j.enggeo.2008.12.002

Zeng, C. Q., Zhang, W. Y., Ma, Q., and Wen, S. J. (2022). Experimental study on the stiffness degradation of remolded loess in Haibei area under cyclic loading. *J. Earthq. Eng.* 44, 292–298. doi:10.20000/j.1000-0844.20200617004

Zhang, Y. W., Song, Z. P., and Weng, X. L. (2022). A constitutive model for loess considering the characteristics of structurality and anisotropy. *Soil Mech. Found. Eng.* 59, 32–43. doi:10.1007/s11204-022-09781-z

Zhuang, J. Q., Peng, J. B., Xu, C., Li, Z., Densmore, A., Milledge, D., et al. (2018). Distribution and characteristics of loess landslides triggered by the 1920 haiyuan earthquake, northwest of China. *Geomorphology* 314 (6), 1–12. doi:10.1016/j.geomorph.2018.04.012